

Article

The Activation Mechanism of Bi^{3+} Ions to Rutile Flotation in a Strong Acidic Environment

Wei Xiao ^{1,2}, Pan Cao ^{1,2}, Qiannan Liang ^{1,2}, Hong Peng ³, Hongbo Zhao ^{1,2}, Wenqing Qin ^{1,2}, Guanzhou Qiu ^{1,2} and Jun Wang ^{1,2,*}

¹ School of Minerals Processing & Bioengineering, Central South University, Changsha 410083, China; xiaowei2015@yahoo.com (W.X.); caopan@csu.edu.cn (P.C.); lqn2018@163.com (Q.L.); alexandercsu@126.com (H.Z.); qinwenqingcsu@126.com (W.Q.); qgz@csu.edu.cn (G.Q.)

² Key Lab of Biohydrometallurgy of Ministry of Education, Changsha 410083, China

³ School of Chemical Engineering, The University of Queensland, Brisbane, Queensland 4072, Australia; h.peng2@uq.edu.au

* Correspondence: wjwq2000@126.com; Tel.: +86-0731-8887-6557

Received: 8 June 2017; Accepted: 28 June 2017; Published: 2 July 2017

Abstract: Lead hydroxyl compounds are known as rutile flotation of the traditional activated component, but the optimum pH range for flotation is 2–3 using styryl phosphoric acid (SPA) as collector, without lead hydroxyl compounds in slurry solution. In this study, Bi^{3+} ions as a novel activator was investigated. The results revealed that the presence of Bi^{3+} ions increased the surface potential, due to the specific adsorption of hydroxyl compounds, which greatly increases the adsorption capacity of SPA on the rutile surface. Bi^{3+} ions increased the activation sites through the form of hydroxyl species adsorbing on the rutile surface and occupying the steric position of the original Ca^{2+} ions. The proton substitution reaction occurred between the hydroxyl species of Bi^{3+} ions ($\text{Bi}(\text{OH})_n^{+(3-n)}$) and the hydroxylated rutile surface, producing the compounds of Ti-O-Bi^{2+} . The micro-flotation tests results suggested that Bi^{3+} ions could improve the flotation recovery of rutile from 61% to 90%, and from 61% to 64% for Pb^{2+} ions.

Keywords: rutile activation flotation; styryl phosphoric acid; Strong acidic environment; activation sites; hydroxyl compound

1. Introduction

Rutile is the best raw material for high-end titanium pigment production and a high grade titanium to extract, which has important implications for the defense industry and high-end coating market [1,2]. The majority of rutile ores belong to refractory ores, and its concentration is very difficult due to their fine grain sizes associated with the gangues, the complexity of the mineralogy, and the brittleness to easily over-ground [3]. Although the concentration of rutile ores is obtained by a combination of gravity, magnetic and electrostatic separation techniques, flotation is one of the most efficient methods to solve the issue [4].

Sodium oleate, water-soluble petroleum sulfonate, styryl phosphoric acid (SPA), benzyl arsenic acid, alkyl imino bismethylene phosphoric acid and hydroxamic acid are commonly used as collectors in rutile flotation [5–7]. Liu and Peng [5] thought SPA was considered to be the most selective collector for rutile, but high consumption has limited its use. So, we investigated some activators to enhance the flotation effects of SPA. Many studies have reported that $\text{Pb}(\text{NO}_3)_2$ was the effective activator to the flotation of the minerals containing titanium. Li et al. [8] found that $\text{Pb}(\text{NO}_3)_2$ was an activator to effectively improve rutile floatability using salicyl hydroxamic acid as a collector, and the optimal pH range for the activating processing was 5.5–6.8. Fan and Rowson [9] investigated the effects of $\text{Pb}(\text{NO}_3)_2$ on the flotation separation of ilmenite using sodium oleate as a collector. They found that

ilmenite could be activated by $\text{Pb}(\text{NO}_3)_2$ in the pH range of 4–8, but that it would be reduced when the pH range was 2–3.

Two mechanisms of metal ions adsorption in the activation of minerals have been proposed: (1) the formation of $\text{Me}_1\text{-O-Me}_2^+$ species (Me_1 : Zn, Mn, Fe, Sn, etc.; Me_2 : Pb^{2+} and Cu^{2+}), which are the product of complex interactions between $\text{Me}_2(\text{OH})^+$ and the mineral surface [9]; (2) the formation of Me_2S or Me_2O by the exchange of Me_2 and Me_1 [10–12]. However, these two mechanisms are just possible under certain conditions. The condition of mechanism (1) is the formation of hydroxy compounds of Me_2 ; and (2) is that the solubility product of Me_2S or Me_2O needs to be less than that of Me_1S or Me_1O . However, in the pH range of 1–3, the main specie of $\text{Pb}(\text{NO}_3)_2$ in the solution is free Pb^{2+} ions and is adsorbed on the rutile surface through electrostatic forces [8], and the solubility product of PbO is much greater than TiO_2 . So, Pb^{2+} ions have been unable to act as an activator for rutile flotation in this pH range.

It was reported that the Bi^{3+} and Pb^{2+} ions had lone pairs of electrons, which could be stereochemically active, and exert a considerable effect on the structures of their complexes [13,14]. Bi^{3+} ions readily hydrolyze in aqueous solutions ($\text{pK}_a = 1.51$) and have a high affinity to both oxygen and nitrogen ligands [13,15]. These have two implications for us: (1) Bi^{3+} ions have the same functional configuration with respect to the activation of Pb^{2+} ions; (2) Bi^{3+} ions have been hydrolyzed in the optimal flotation pH of 2–3.

We found that Bi^{3+} ions could significantly improve the recovery rate of rutile flotation in pure minerals. In this study, the activation mechanism of Bi^{3+} ions to rutile flotation and its subsequent flotation response to styryl phosphoric acid (SPA) were investigated as a novel activator to rutile flotation by micro-flotation tests, zeta potential measurements, adsorption capacity measurements and X-ray photoelectron spectroscopy (XPS) analyses. The activation mechanism of Bi^{3+} ions to rutile flotation was discussed. The presented results are expected to be useful for the development and selection of high efficiency activators for rutile flotation.

2. Materials and Methods

2.1. Materials

Rutile samples used in this study were obtained from Zaoyang Mine, Hubei province, China. The samples were crushed and ground to particle size from 38 to 74 μm , and were then purified by sieving, several stages of tabling, and low and high intensity magnetic separation methods. The pure rutile samples were washed several times with distilled water and dried at room temperature. The result of particle size analysis was shown in Figure 1. The average particle size of rutile was 53.98 μm measured by a laser particle size analyzer (Mastersizer 2000, Malvern Instruments Ltd., Malvern, UK). Examination under an ultrasonic generator showed rutile grains had a clean surface, and were almost free from gangue minerals. All of the reagents are analytically pure grade in this study.

The crystal phase composition was determined by X-ray diffraction XRD (Germany Bruker-axes D8 Advance, Karlsruhe, Germany), whose detailed processes and methods were previously described by Han [16]. The chemical composition of rutile was carried out by a wavelength dispersive X-ray Fluorescence (XRF, PANalytical B.V., Almelo, The Netherlands) spectrometer S4 Pioneer. The results of XRD and XRF are shown in Figure 2 and Table 1. The XRD results in Figure 2 demonstrate that the rutile samples were mainly composed of rutile, and the Ti element was only originated from rutile mineral. So, according to element content of XRF results in Table 1, the purity of rutile mineral in the sample was calculated to be 93.8%.

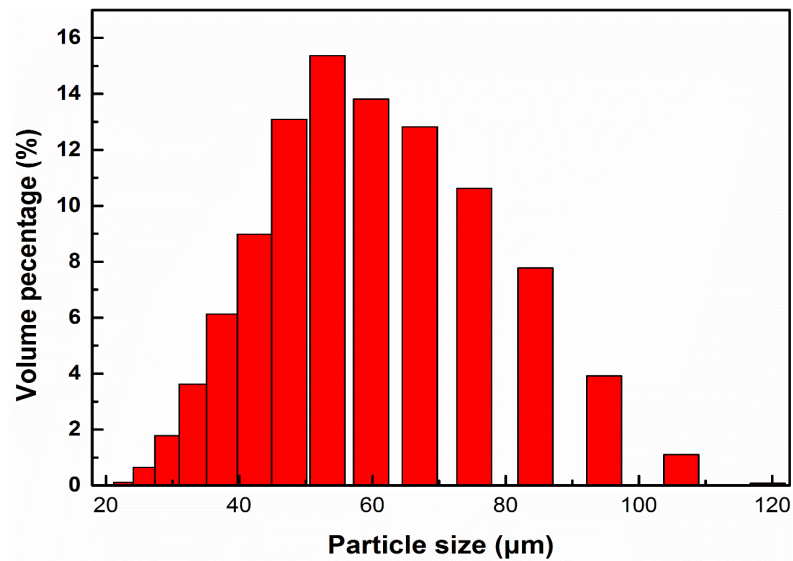


Figure 1. Size contribution of rutile sample.

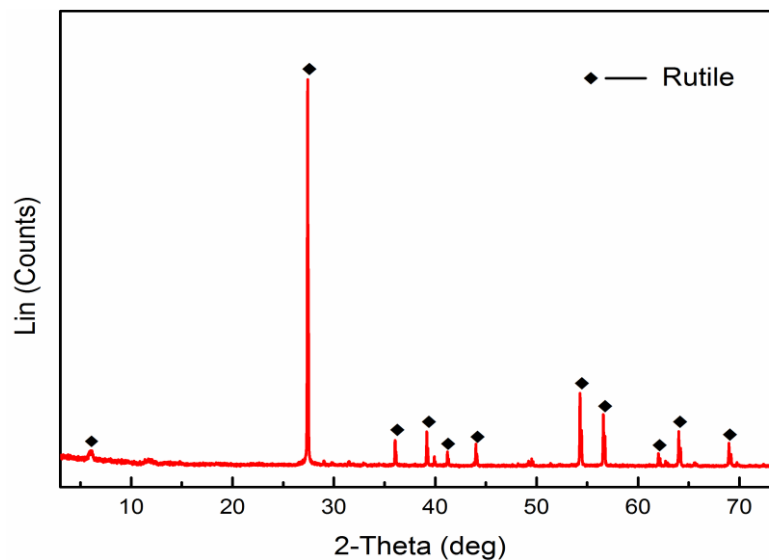


Figure 2. XRD pattern of rutile.

Table 1. Multi-element analysis of pure rutile mineral (%).

Element	TiO ₂	FeO	Fe ₂ O ₃	SiO ₂	CaO	MgO	Al ₂ O ₃
Content	93.80	1.53	1.33	2.17	0.17	0.31	0.99

2.2. Methods

2.2.1. Micro-Flotation Tests

The purified mineral particles (2 g) were placed in a plexiglass cell (40 mL), which was then filled with distilled water and the pH value was adjusted. After keeping for 2 min, the metal ions and the collector were added, respectively. The suspension was agitated for 2 and 3 min, respectively. The pH was measured before the flotation, and the flotation was conducted for 4 min. The concentrates were weighed after filtration and drying, and the recovery rate was then calculated.

2.2.2. Adsorption Experiments

The treatment of rutile samples, the time and order of addition of the reagents were the same as micro-flotation tests, except that the flotation was not carried out. The suspension was agitated for 5 min. After each step of the extraction process the samples were centrifuged and filtered to separate the liquid and solid phases. After washing twice with distilled water, the filter liquor was moved to a 100-mL volumetric flask. The adsorption amount was calculated by following Equation (1):

$$Q_e = \frac{V(C_0 - C_e)}{WS} \quad (1)$$

where, Q_e is the amount of SPA adsorbed on the surface of rutile (mol/m^2), C_0 is the initial concentration of SPA (mol/L), V is the volume (L), S is the specific surface area of rutile (m^2/g), and W is the mass of rutile (g).

2.2.3. Zeta Potential Measurements

The zeta potential of rutile surface was measured using a ZetaPALS instrument (Brookhaven, MS, USA). The samples were ground to less than 5 μm . The suspension was prepared by adding 50 mg of pure rutile to 5 mL of distilled, deionized water containing 10^{-3} mol/L KCl as a supporting electrolyte. The resulting suspension was conditioned for 15 min during which suspension pH was measured. The pH was adjusted using either NaOH or H_2SO_4 over the pH range of 2–12.

2.2.4. X-ray Photoelectron Spectroscopy

The chemical compositions of rutile surfaces were determined by XPS on a Thermo Scientific ESCALAB 250Xi (Thermo Fisher Scientific, Waltham, MA, USA) using Al $K\alpha$ X-ray source operated at 200 W with 20 eV pass energy. The vacuum pressure was ranged from 10^{-9} to 10^{-8} Torr and the takeoff angle was 90° . The data were collected and analyzed using the method under Thermo Scientific Avantage 4.52 software [17,18].

3. Results and Discussion

3.1. Micro-Flotation Tests

The flotation recoveries of rutile as a function of pH using SPA as collector are shown in Figure 3. In this study, Bi^{3+} and Pb^{2+} ions were added as the activators. Figure 3 shows that without the addition of Bi^{3+} and Pb^{2+} ions, the recovery of rutile is low (around 61%), and the optimal pH range of rutile flotation is 1–2. With the addition of Pb^{2+} ions, the recovery of rutile slightly improves (around 65%), and the optimal pH range of rutile flotation is 1–2.7. With the addition of Bi^{3+} ions, the recovery of rutile sharply increases (around 90%), and the optimal pH range of rutile flotation is 1–3.

Figure 4 shows Δ flotation recovery before and after the addition of activation ions as a function of pH. The Δ flotation recovery represents the activation ability of Pb^{2+} and Bi^{3+} ions on rutile flotation. It suggested that the activation ability of metal ions to rutile flotation improved with the different increase. The addition of Pb^{2+} ions increased the rutile recovery when the pH was from 1 to 8. In strongly acidic conditions ($\text{pH} < 2.5$), the recovery of rutile was improved slightly (Δ 1 less than 5%), while in $\text{pH} > 2.5$, there was a great change (Δ 1 more than 15%). It indicated that Pb^{2+} ions could not be used as the activator for rutile flotation in the pH range of 1–2.5, but could be used as the activator in the pH range of 2.5–7.0. Li et al. [8] used Pb^{2+} ions as the activator for rutile flotation with the collector of salicyl hydroxamic acid (SHA) in the pH range of 4.5–6.5, which was similar to our results.

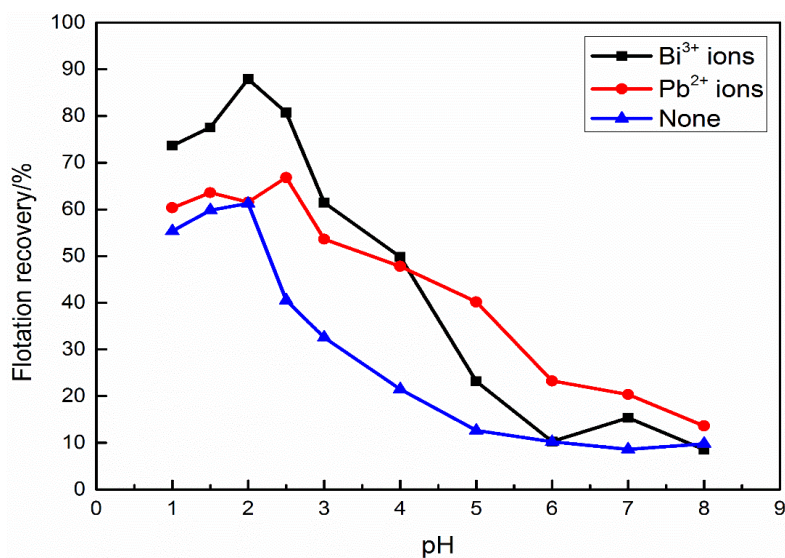


Figure 3. The flotation recovery of rutile as a function of pH in the presence of 600 mg/L styryl phosphoric acid (SPA): $[\text{Bi}^{3+}] = 10^{-5}$ mol/L; $[\text{Pb}^{2+}] = 10^{-4}$ mol/L.

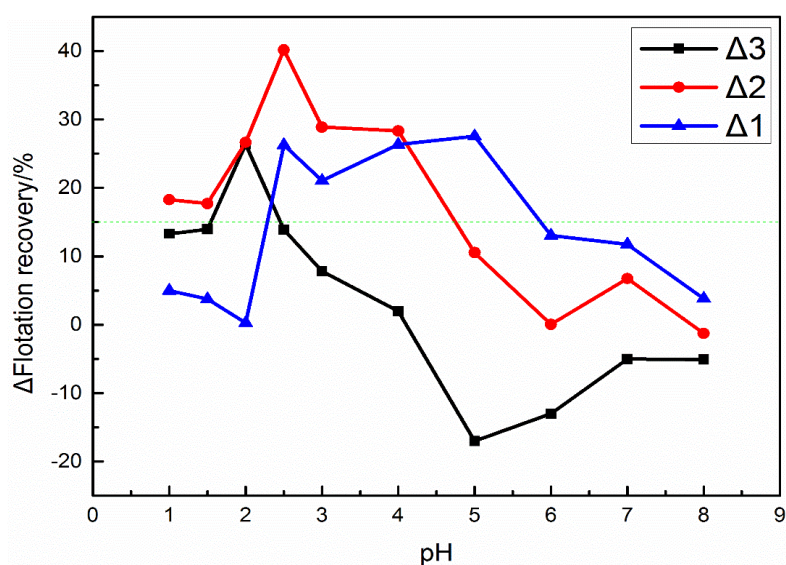


Figure 4. The Δ flotation recovery as a function of pH: $\Delta 1$ is the difference before and after Pb^{2+} ions addition; $\Delta 2$ is the difference before and after Bi^{3+} ions addition; $\Delta 3$ is the difference between Pb^{2+} and Bi^{3+} ions.

The addition of Bi^{2+} ions increased the rutile recovery when the pH was from 1 to 6. In strongly acidic conditions ($\text{pH} < 4.8$), the recovery of rutile improved sharply ($\Delta 2$ more than 15%), while $\text{pH} > 6.0$, there was slight change ($\Delta 2$ less than 5%). It suggested that Bi^{2+} ions can be used as the activator for rutile flotation in the pH range of 1–4.8, especially at pH 2.5, when $\Delta 2$ reaches the greatest value (about 40%), indicating that the activation ability was strongest at pH 2.5.

The $\Delta 3$ represents the difference of the activation ability of Pb^{2+} and Bi^{3+} ions on rutile flotation. Figure 4 shows that $\Delta 3$ was more than zero when $1.0 < \text{pH} < 4.0$, and less than zero when $4.0 < \text{pH} < 8.0$. It indicated that the activation ability of Bi^{3+} ions was stronger than Pb^{2+} ions when $1.0 < \text{pH} < 4.0$, and weaker when Pb^{2+} ions when $4.0 < \text{pH} < 8.0$.

The concentration of Ca^{2+} ions in the pulp solution as a function of pH is shown in Figure 5. Figure 5 shows that the concentration of Ca^{2+} ions in the pulp solution increased with the pH value declining, especially in the pH range of 1–2, when the concentration of Ca^{2+} ions increased sharply. It indicated that the calcium impurity on the rutile surface was dissolved in the acidic conditions, especially in the pH range of 1–2, when it dissolved the most obviously. Combined with the curve of flotation recovery, without activation ions, the flotation recovery of the rutile decreased slightly with the pH value decreasing when the pH was 1–2. That was because the activating sites on rutile surface were dissolved to aqueous solution in the condition of strongly acidic conditions ($\text{pH} < 2.0$) [19,20]. The flotation recovery of the rutile decreased slightly due to SPA adsorbed on the active sites of calcium, which made it more difficult. Table 2 shows that the radius of Ca^{2+} ions was very close to the radius of Bi^{3+} ions, less than that of Pb^{2+} ions [21]. It indicated that Bi^{3+} ions can easily occupy the position of the original Ca^{2+} ions on rutile surface, but that is was very difficult for Pb^{2+} ions to occupy the vacancy left by Ca^{2+} ions dissolution, due to the large radius and the steric hindrance. Since the Bi^{3+} ions were +3 valences, it occupied the position of Ca^{2+} ions, and it was still expressed as +1 valences, which was favorable for the adsorption of the anions of SPA on the substituted Bi^{3+} ions sites. It explained the phenomenon that the flotation recovery and the adsorption capacity of SPA increased sharply in the presence of Bi^{3+} ions in the pH range of 1–2.

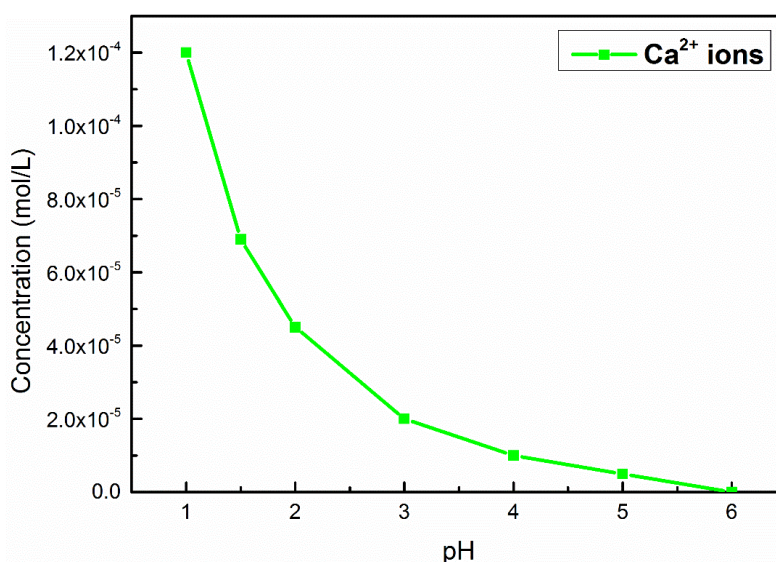


Figure 5. The concentration of Ca^{2+} ions as a function of pH.

Table 2. The radius of metal ions (All are 6 coordinated).

Ions type	Ca^{2+}	Fe^{2+}	Fe^{3+}	Mg^{2+}	Al^{3+}	Pb^{2+}	Bi^{3+}
Radius (Å)	1.14	0.92	0.785	0.86	0.675	1.33	1.17

3.2. Adsorption Amount of SPA

The adsorption amount of SPA on rutile surface in the presence and absence of Bi^{3+} ions and Pb^{2+} ions as a function of pH is presented in Figure 6. Figure 6 shows the optimal pH range of SPA adsorption was 1–2 without activation ions. With the addition of Pb^{2+} ions, the adsorption amount of SPA on rutile surface changed slightly in the optimal pH range, but with the addition of Bi^{3+} ions, the adsorption amount of SPA increased sharply in the optimal pH range, which was very consistent with the flotation recovery. It suggested that the adsorption amount of SPA was a key factor to determine the flotation recovery. With the increase of adsorption amount of the collector, the hydrophobicity of mineral surface increased, and led to the floatability of mineral improved [22–24].

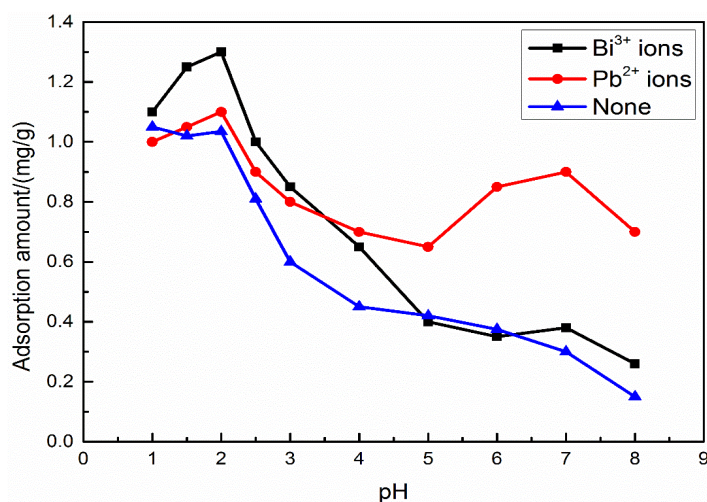


Figure 6. The adsorption amount of SPA on rutile surfaces before and after Bi³⁺ ions modification as a function of pH.

3.3. Zeta Potentials

Adsorption of cations onto a mineral inevitably leads to a change in the surface charge. Figure 7 shows the zeta potentials of rutile as a function of pH in different conditions. In the absence of activators, the point of zero charge (PZC) of rutile occurred at $\text{pH } 3.8 \pm 0.1$, which was almost in accord with the previous values reported by Parks [25]. In the presence of 10^{-4} mol/L Pb²⁺ ions, the zeta potentials of rutile particles moved to more positive values and the PZC appeared at about $\text{pH } 9.0 \pm 0.1$. In the presence of 10^{-5} mol/L Bi³⁺ ions, the PZC appeared at about $\text{pH } 4.5 \pm 0.1$.

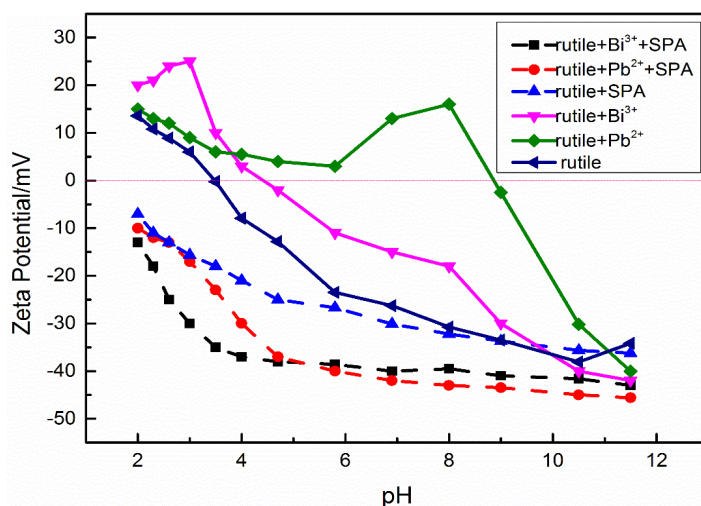


Figure 7. Zeta potential of rutile surface with a function of pH.

Figure 8 shows that the zeta potentials of the rutile surface were affected slightly by Pb²⁺ ions in the pH range of 2–4. At $\text{pH } < 4.0$, and all of the lead nitrate in the solution were present as free ions. The species distribution diagrams for Bi³⁺, Pb²⁺, Ti⁴⁺ ions and SPA are shown in Figure 9 and help explain the results obtained from zeta potential experiments [19]. On one hand, Pb²⁺ ions adsorbed on the rutile surface through electrostatic forces [8], resulting in the increase of zeta potential; on the other hand, because of the presence of salt solution, the thickness of the electric double layer of the rutile surface was compressed [26–28], resulting in the decrease of the zeta potential. In the pH range of 1–2.5, which was the optimal pH range for flotation, the rutile surface charge was positive.

The adsorption amount of Pb^{2+} ions on rutile surface was very small [8], which suggested that Pb^{2+} ions could not activate the rutile flotation using SPA as the collector. In the pH range of 5–9, because of the rutile surface with a positive charge, Pb^{2+} ions could easily adsorb on the rutile surface. Figure 9d shows that lead nitrate in solution was primarily present as $\text{Pb}(\text{OH})^+$, primarily present as Pb^{2+} and $\text{Pb}(\text{OH})^+$. While Pb^{2+} decreased with the increase of pH, $\text{Pb}(\text{OH})^+$ increased with increasing pH from 5 to 9. The increased adsorption of lead ions on the rutile surfaces, and more positively charged rutile surfaces from pH 5–9 (Figures 6 and 7), would therefore be attributed to the specific adsorption of $\text{Pb}(\text{OH})^+$ on the rutile surfaces [8,19].

Figure 7 shows that the zeta potentials of the rutile surface dramatically increased in the pH range of 2–4 after the addition of Bi^{3+} ions. In this pH range, bismuth nitrate in solution was primarily as a generation of hydroxyl compounds ($\text{Bi}(\text{OH})^{2+}$) (Figure 9a). The sign of charge on the rutile surface was the same as that of $\text{Bi}(\text{OH})^{2+}$. It indicated that Bi^{3+} ions on the rutile surface facilitated the large specific adsorption in the form of a generation of hydroxyl compounds ($\text{Bi}(\text{OH})^{2+}$). In the optimum flotation range, the adsorption of metal cations on the mineral surface brought two advantages to the flotation process: (1) the zeta potentials of the mineral surface dramatically increased after the metal cations adsorption, which was better for the adsorption of anionic collectors on the mineral surface; (2) the metal cations adsorbed on the mineral surface in the form of the hydroxyl compounds, improved the activation sites for the collector adsorption on the mineral surface.

Figure 7 shows that the zeta potentials of the rutile surface obviously decreased after SPA addition, which indicated that SPA could adsorb on the rutile surface in the presence and absence of activation ions. However, the extent of decline was different. Figure 8 shows Δ zeta potential before and after SPA addition as a function of pH. The Δ zeta potential represented the adsorption capacity of SPA on the rutile surface under different conditions in solution. It suggested that the adsorption capacity of SPA on the rutile surface increased with different increases in activation ions. Figure 8 shows that $\Delta 2$ improved slightly more than $\Delta 1$, and $\Delta 3$ dramatically increased in comparison to $\Delta 1$ and $\Delta 2$ in the pH range of 2–3. It indicated that the effect of Pb^{2+} ions on SPA adsorption was very small, and the adsorption capacity of SPA on the rutile surface dramatically increased in the presence of Bi^{3+} ions.

The presence of Bi^{3+} ions increased the surface potential, and facilitated the large specific adsorption in the form of the hydroxyl compounds, which greatly increased the adsorption capacity of SPA on the rutile surface, thus improving the hydrophobicity of the rutile surface, resulting in an increase in flotation recovery.

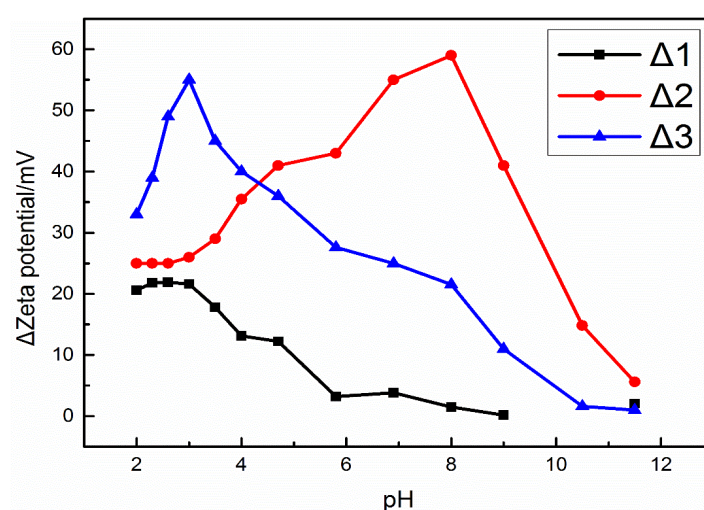


Figure 8. Δ Zeta potential of rutile surface with a function of pH: $\Delta 1$ is the difference before and after SPA addition without activation ions; $\Delta 2$ is the difference before and after SPA addition with Pb^{2+} ions; $\Delta 3$ is the difference before and after SPA addition with Bi^{3+} ions.

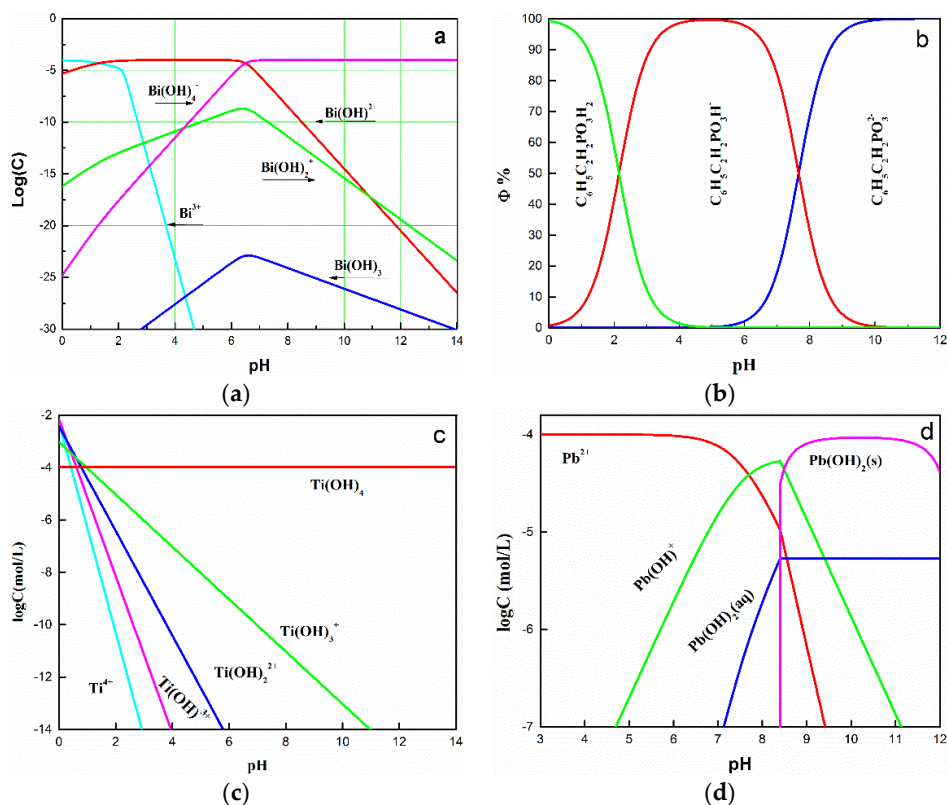


Figure 9. The percentage distribution of Bi^{3+} ions (a), SPA (b) species, Ti^{4+} ions (c) and Pb^{2+} ions (d) as a function of pH values.

3.4. XPS Analysis

The composition of the rutile surface after Bi^{3+} ions adsorption was investigated by XPS. Figure 10 shows the survey scan and high-resolution XPS spectra of the rutile after Bi^{3+} ions adsorption. An obvious peak at about 162 eV was showed in Figure 10a, which indicated that Bi^{3+} ions could adsorb on the rutile surface in the form of a compound. The high-resolution XPS spectra of O, Ti and Bi elements were scanned in order to extract the information of the chemical states. The curve-fit results are shown in Figure 10b,c, respectively, and their XPS peak parameters and chemical states are presented in Table 3.

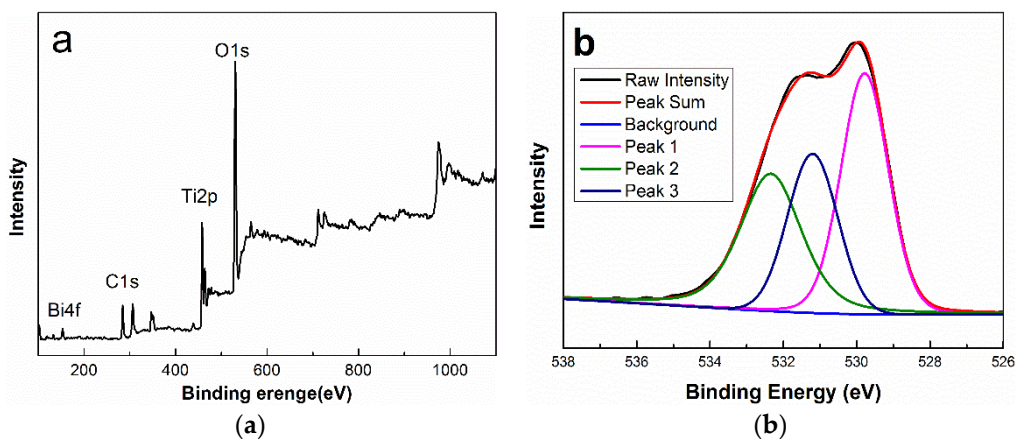


Figure 10. Cont.

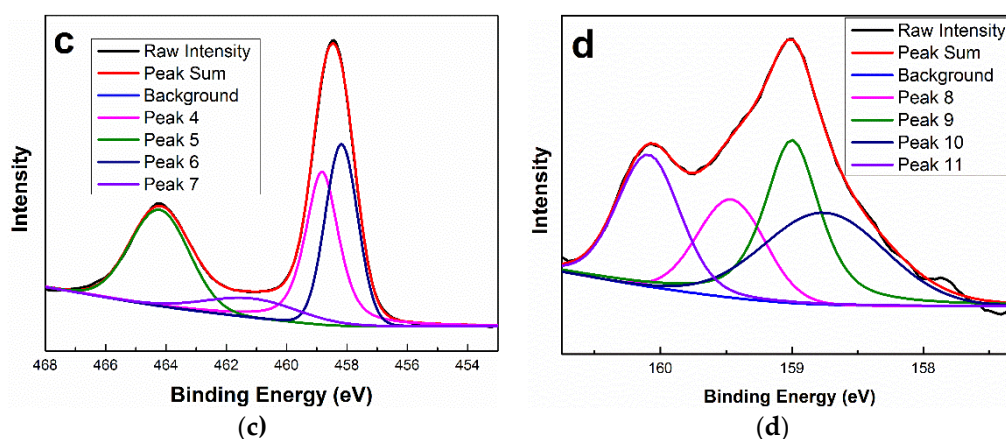


Figure 10. The survey scan and high-resolution X-ray photoelectron spectroscopy (XPS) Spectra of rutile after Bi^{3+} ions adsorption ($[\text{Bi}^{3+}] = 10^{-5}$ mol/L): (a) the survey scan spectra; (b) curve-fitted O 1s XPS spectra; (c) curve-fitted Ti 2p XPS spectra; (d) curve-fitted Bi $4f_{5/2}$ XPS spectra.

Table 3. The O 1s, Ti 2p, and Bi $4f_{5/2}$ XPS parameters and chemical states for rutile after Bi^{3+} ions adsorption.

Atom Orbit	Peak	Binding Energy (eV)	Chemical States
O 1s	Peak 1	531.19	Ti-O-Bi (rutile surface)
	Peak 2	532.34	hydroxyl species (rutile surface)
	Peak 3	529.79	Ti-O-Ti (rutile bulk)
Ti 2p	Peak 4	458.84	O-Ti-O (Ti $2p_{3/2}$) (rutile bulk)
	Peak 5	464.24	O-Ti-O (Ti $2p_{1/2}$) (rutile bulk)
	Peak 6	458.19	Ti-OH (rutile surface)
	Peak 7	461.19	Ti-O- Bi^{2+} (rutile surface)
Bi $4f_{7/2}$	Peak 8	159.47	hydroxyl compounds (rutile surface)
	Peak 9	158.99	hydroxyl compounds (rutile surface)
	Peak 10	158.74	hydroxyl compounds (rutile surface)
	Peak 11	160.10	Ti-O- Bi^{2+} (rutile surface)

The detailed scan spectrum of O 1s is presented in Figure 10b and composed of three components. As shown in Table 3, peak 3 was assigned to the O^{2-} state in rutile bulk (529.72 eV) [21,29], and peak 2 was assigned to the O^{2-} state in hydroxyl species on the rutile surface [30], including Ti-OH and Bi-OH (532.34 eV). It indicated that the hydroxylation process was present on rutile surface. Peak 1 was tentatively assigned to the O^{2-} state in Ti-O-Bi on the rutile surface (531.19) [21].

The detailed scan spectrum of Ti 2p is presented in Figure 10c and composed of two components. The characteristic of peaks 5 (464.24 eV) and 4 (458.19 eV) was obviously attributed to the XPS spectrum of Ti 2p in rutile bulk [8,31,32]. Combined with the previous analysis, peak 4 (458.84 eV) and peak 7 (461.19 eV) were tentatively assigned to the Ti^{4+} states in Ti-OH and Ti-O- Bi^{2+} on the surface of rutile.

The detailed scan spectrum of Bi $4f_{7/2}$ is presented in Figure 10d and composed of four components. As shown in Table 3, Peaks 8, 9 and 10 were assigned to the Bi $4f_{7/2}$ of hydroxyl compounds of Bi^{3+} ions, which agreed well with the results in the literature [33]. This was very consistent with the previous results, which suggested that Bi^{3+} ions adsorbed on the rutile surface in the form of hydroxides. Peak 11 had a binding energy of 160.10 eV, which was higher than that of the Bi^{3+} states in hydroxyl compounds. It may be due to the formation of the complex of Ti-O- Bi^{2+} on the rutile surface, because the complex of Ti-O- Bi^{2+} was present, as Peak 2 proved.

At pH 2.0, Bi^{3+} ions in the form of the hydroxyl species ($\text{Bi}(\text{OH})_n^{+(3-n)}$) chemically interacted with the Ti-OH on rutile surface (after hydroxylation), forming the surface complex of Ti-O- Bi^{2+} .

4. Conclusions

The presence of Bi^{3+} ions increases the surface potential, and facilitates the large specific adsorption in the form of hydroxyl compounds, which greatly increases the adsorption capacity of SPA on rutile surface, thereby improving the hydrophobicity of the rutile surface, resulting in an increase in flotation recovery. The activation mechanism of Bi^{3+} ions to rutile flotation is proposed by Figure 11, and the following conclusions can be drawn.

- (1) The calcium impurity on the rutile surface is dissolved in strongly acidic conditions, and Bi^{3+} ions occupy the steric position of the original Ca^{2+} ions (in Figure 11A).
- (2) The proton substitution reaction occurs between the hydroxyl species of Bi^{3+} ions and hydroxylated rutile surface, producing the compounds of Ti-O-Bi^{2+} (in Figure 11B).
- (3) Bi^{3+} ions can adsorb on the rutile surface in the form of hydroxyl species, and increased the activation sites on the rutile surface (in Figure 11C).

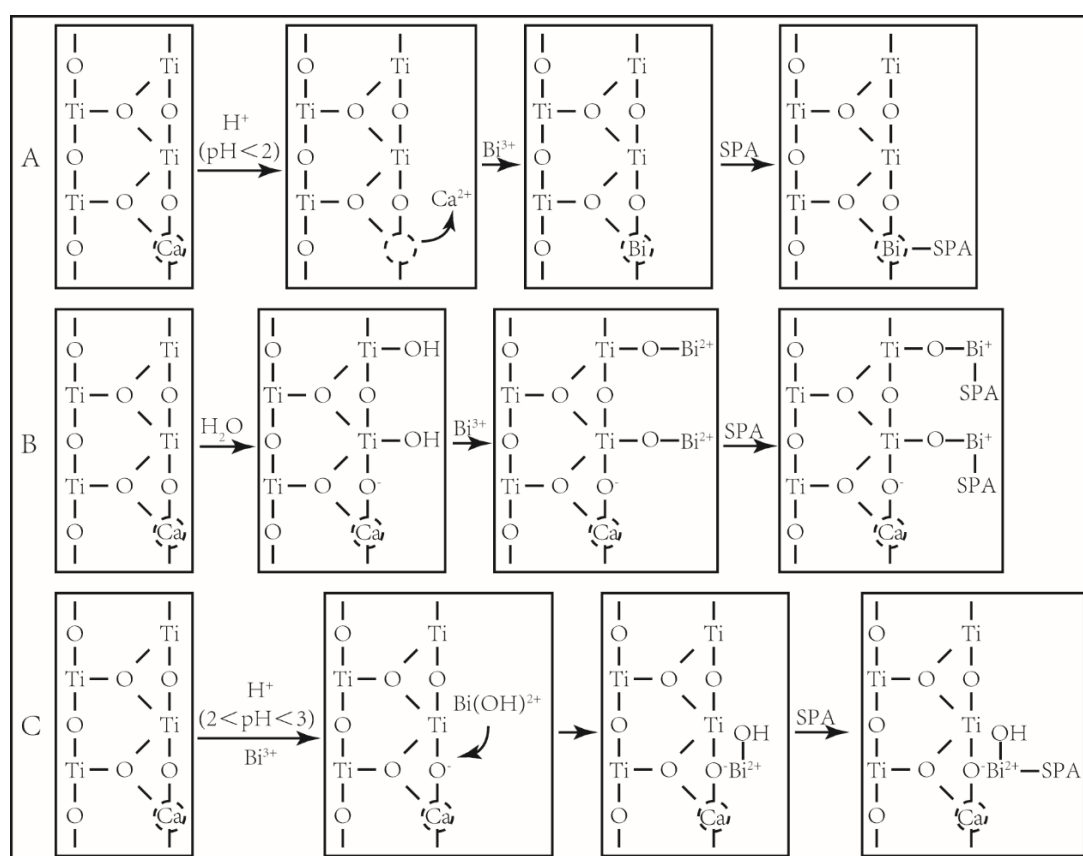


Figure 11. The models of the activation mechanism of Bi^{3+} to rutile flotation. (A): Occupying the vacancy left by Ca^{2+} ions dissolution; (B): the proton substitution reaction; (C): increasing the activation sizes in the form of hydroxyl species.

Acknowledgments: The authors acknowledge the financial support of the National Natural Science Foundation of China (No. 51474254), China Postdoctoral Science Foundation (No. 2013M531813), the Independent Exploration and Innovation Projects of Doctor (No. 2016zzts111) and Master (No. 2016zzts468) of Central South University and the Open-End Fund for Valuable and Precision Instruments of Central South University (No. CSUZC201715).

Author Contributions: Wei Xiao and Jun Wang conceived of and designed the experiments; Qiannan Liang and Pan Cao prepared the samples and performed the experiments; Wei Xiao and Pan Cao analyzed the data. Wei Xiao, Hong Peng, Hongbo Zhao, Wenqing Qin, and Guanzhou Qiu contributed to the writing and revising of the paper.

Conflicts of Interest: The authors declare no conflict of interest.

References

1. Li, T.; Wu, Y.; Wang, Q.; Zhang, D.; Zhang, A.; Miao, M. TiO₂ crystalline structure and electrochemical performance in two-ply yarn CNT/TiO₂ asymmetric supercapacitors. *J. Mater. Sci.* **2017**, *52*, 7733–7743. [[CrossRef](#)]
2. Nam, I.; Park, J.; Park, S.; Bae, S.; Yoo, Y.G.; Han, J.W.; Yi, J. Observation of crystalline changes of titanium dioxide during lithium insertion by visible spectrum analysis. *Phys. Chem. Chem. Phys.* **2017**, *19*, 13140–13146. [[CrossRef](#)] [[PubMed](#)]
3. Chachula, F.; Liu, Q. Upgrading a rutile concentrate produced from Athabasca oil sands tailings. *Fuel* **2003**, *82*, 929–942. [[CrossRef](#)]
4. Wang, J.; Cheng, H.W.; Zhao, H.B.; Qin, W.Q.; Qiu, G.Z. Flotation behavior and mechanism of rutile with nonyl hydroxamic acid. *Rare Met.* **2016**, *35*, 419–424. [[CrossRef](#)]
5. Liu, Q.; Peng, Y. The development of a composite collector for the flotation of rutile. *Miner. Eng.* **1999**, *12*, 1419–1430. [[CrossRef](#)]
6. Madeley, J.D.; Graham, K. Flotation of rutile with anionic and cationic collectors. *J. Appl. Chem.* **2010**, *16*, 169–170. [[CrossRef](#)]
7. Peng, Y. Effect of interactions between styryl phosphoric acid and aliphatic alcohol on rutile flotation. *Chin. J. Nonferrous Metals* **1999**, *9*, 358–361.
8. Li, H.; Mu, S.; Weng, X.; Zhao, Y.; Song, S. Rutile Flotation with Pb²⁺ Ions as Activator: Adsorption of Pb²⁺ at Rutile/Water Interface. *Colloids Surf. A Physicochem. Eng. Asp.* **2016**, *506*, 431–437. [[CrossRef](#)]
9. Fan, X.; Rowson, N.A. The effect of Pb(NO₃)₂ on ilmenite flotation. *Miner. Eng.* **2000**, *13*, 205–215. [[CrossRef](#)]
10. Albrecht, T.W.J.; Addai-Mensah, J.; Fornasiero, D. Critical copper concentration in sphalerite flotation: Effect of temperature and collector. *Int. J. Miner. Process.* **2016**, *146*, 15–22. [[CrossRef](#)]
11. Chandra, A.P.; Puskar, L.; Simpson, D.J.; Gerson, A.R. Copper and xanthate adsorption onto pyrite surfaces: Implications for mineral separation through flotation. *Int. J. Miner. Process.* **2012**, *114–117*, 16–26. [[CrossRef](#)]
12. Han, J.; Liu, W.; Qin, W.; Zhang, T.; Chang, Z.; Xue, K. Effects of sodium salts on the sulfidation of lead smelting slag. *Miner. Eng.* **2017**, *108*, 1–11. [[CrossRef](#)]
13. Luckay, R.; Cukrowski, I.; Mashishi, J.; Reibenspies, J.H.; Bond, A.H.; Rogers, R.D.; Hancock, R.D. Synthesis, stability and structure of the complex of bismuth(III) with the nitrogen-donor macrocycle 1,4,7,10-tetraazacyclododecane. The role of the lone pair on bismuth(III) and lead(II) in determining coordination geometry. *J. Chem. Soc. Dalton Trans.* **1997**, *5*, 901–908. [[CrossRef](#)]
14. Gillespie, R.J.; Nyholm, R.S.Q. Inorganic stereochemistry. *Q. Rev. Chem. Soc.* **1957**, *11*, 339–380. [[CrossRef](#)]
15. Yang, N.; Sun, H. Biocoordination chemistry of bismuth: Recent advances. *Coord. Chem. Rev.* **2007**, *251*, 2354–2366. [[CrossRef](#)]
16. Han, J.; Jiao, F.; Liu, W.; Qin, W.; Xu, T.; Xue, K.; Zhang, T. Innovative Methodology for Comprehensive Utilization of Spent MgO-Cr₂O₃ Bricks: Copper Flotation. *ACS Sustain. Chem. Eng.* **2016**, *4*, 5503–5510. [[CrossRef](#)]
17. Zhao, H.; Wang, J.; Gan, X.; Hu, M.; Tao, L.; Qiu, G. Role of pyrite in sulfuric acid leaching of chalcopyrite: An elimination of polysulfide by controlling redox potential. *Hydrometallurgy* **2016**, *164*, 159–165. [[CrossRef](#)]
18. Wang, J.; Gan, X.; Zhao, H.; Hu, M.; Li, K.; Qin, W.; Qiu, G. Dissolution and passivation mechanisms of chalcopyrite during bioleaching: DFT calculation, XPS and electrochemistry analysis. *Miner. Eng.* **2016**, *98*, 264–278. [[CrossRef](#)]
19. Liu, W.; Zhang, S.; Wang, W.; Zhang, J.; Yan, W.; Deng, J.; Feng, Q.; Huang, Y. The effects of Ca(II) and Mg(II) ions on the flotation of spodumene using NaOL. *Miner. Eng.* **2015**, *79*, 40–46. [[CrossRef](#)]
20. Fornasiero, D.; Ralston, J. Cu(II) and Ni(II) activation in the flotation of quartz, lizardite and chlorite. *Int. J. Miner. Process.* **2005**, *76*, 75–81. [[CrossRef](#)]
21. Bagwasi, S.; Niu, Y.; Nasir, M.; Tian, B.; Zhang, J. The study of visible light active bismuth modified nitrogen doped titanium dioxide photocatalysts: Role of bismuth. *Appl. Surf. Sci.* **2013**, *264*, 139–147. [[CrossRef](#)]
22. Qin, W.; Jiao, F.; Sun, W.; Wang, X.; Liu, B.; Wang, J.; Zeng, K.; Wei, Q.; Liu, K. Effects of sodium salt of *N,N*-dimethyldi-thiocarbamate on floatability of chalcopyrite, sphalerite, marmatite and its adsorption properties. *Colloids Surf. A Physicochem. Eng. Asp.* **2013**, *421*, 181–192. [[CrossRef](#)]
23. Leppinen, J.O. FTIR and flotation investigation of the adsorption of ethyl xanthate on activated and non-activated sulfide minerals. *Int. J. Miner. Process.* **1990**, *30*, 245–263. [[CrossRef](#)]

24. Jiang, H.; Sun, Z.; Xu, L.; Hu, Y.; Huang, K.; Zhu, S. A comparison study of the flotation and adsorption behaviors of diaspore and kaolinite with quaternary ammonium collectors. *Miner. Eng.* **2014**, *65*, 124–129. [[CrossRef](#)]
25. Parks, G.A. The Isoelectric Points of Solid Oxides, Solid Hydroxides, and Aqueous Hydroxo Complex Systems. *Chem. Rev.* **1965**, *65*, 177–198. [[CrossRef](#)]
26. Yu, X.; Ruan, D.; Wu, C.; Jing, W.; Shi, Z. Spiro-(1,1′)-bipyrrolidinium tetrafluoroborate salt as high voltage electrolyte for electric double layer capacitors. *J. Power Sources* **2014**, *265*, 309–316. [[CrossRef](#)]
27. Han, T.; Park, M.S.; Kim, J.; Kim, J.H.; Kim, K. The smallest quaternary ammonium salts with ether groups for high-performance electrochemical double layer capacitors. *Chem. Sci.* **2016**, *7*, 1791–1796. [[CrossRef](#)]
28. De Lara, L.S.; Rigo, V.A.; Michelon, M.F.; Metin, C.O.; Nguyen, Q.P.; Miranda, C.R. Molecular dynamics studies of aqueous silica nanoparticle dispersions: Salt effects on the double layer formation. *J. Phys. Condens. Matter* **2015**, *27*. [[CrossRef](#)] [[PubMed](#)]
29. Anitha, B.; Khadar, M.A. Dopant concentration dependent magnetism of Cu-doped TiO₂ nanocrystals. *J. Nanoparticle Res.* **2016**, *18*, 149–164. [[CrossRef](#)]
30. Mikhailova, D.; Karakulina, O.M.; Batuk, D.; Hadermann, J.; Abakumov, A.M.; Herklotz, M.; Tsirlin, A.A.; Oswald, S.; Giebeler, L.; Schmidt, M.; et al. Layered-to-Tunnel Structure Transformation and Oxygen Redox Chemistry in LiRhO₂ upon Li Extraction and Insertion. *Inorg. Chem.* **2016**, *55*, 7079–7089. [[CrossRef](#)] [[PubMed](#)]
31. Bakhshayesh, A.M.; Bakhshayesh, N. Facile one-pot synthesis of uniform niobium-doped titanium dioxide microparticles for nanostructured dye-sensitized solar cells. *J. Electroceramics* **2016**, *36*, 112–121. [[CrossRef](#)]
32. Halpegamage, S.; Wen, Z.H.; Gong, X.Q.; Batzill, M. Monolayer Intermixed Oxide Surfaces: Fe, Ni, Cr, and V Oxides on Rutile TiO₂(011). *J. Phys. Chem. C* **2016**, *120*, 14782–14794. [[CrossRef](#)]
33. Casella, I.G.; Contursi, M. Characterization of bismuth adatom-modified palladium electrodes: The electrocatalytic oxidation of aliphatic aldehydes in alkaline solutions. *Electrochim. Acta* **2006**, *52*, 649–657. [[CrossRef](#)]



© 2017 by the authors. Licensee MDPI, Basel, Switzerland. This article is an open access article distributed under the terms and conditions of the Creative Commons Attribution (CC BY) license (<http://creativecommons.org/licenses/by/4.0/>).